



Trinity College Dublin

Coláiste na Tríonóide, Baile Átha Cliath

The University of Dublin

School of Physics

**Atmospheres of Alien Worlds:
Investigating the Atmospheric Composition
of the Hot-Jupiter Exoplanet WASP-76b via
High Resolution Transmission Spectroscopy**

Jonathan Burke

17327828

March 22, 2021

BA Physics and Astrophysics

Abstract

Extrasolar planets, also known as exoplanets, are planets located outside of our solar system. Exoplanets display a wider range of properties than planets in our own solar system, such as mass, radius, orbital distance, temperature and host star type. Understanding the atmospheric composition of these exoplanets will help provide an insight into planetary formation and migration mechanisms, geophysical processes and may possibly lead to the detection of biosignatures.

As transiting exoplanets periodically eclipse their host star, the effective planetary radius can be measured as a function of wavelength using transmission spectroscopy. Using the large Doppler shift of the exoplanet's spectral signature compared to its host star, the atmospheric composition of these ultra-hot Jupiter exoplanets can be investigated.

This work investigates the atmospheric composition of the exoplanet WASP-76b using data from the ESPRESSO instrument at the VLT. The observational transmission spectra were analysed for the presence of certain chemical species by generating model transmission spectra and searching for them in the observational data, using cross correlation techniques. The species searched for were FeI, NaI, LiI, KI, TiI, MnI, CrI, FeII, MgI, NiI and CaII. For each of these species, models were generated at a range of atmospheric temperatures and with cloud decks located at various altitudes. These models were computed with cross correlation functions for various values of planetary orbital velocity and systemic velocities, in order to obtain the largest detection significance.

From the analysis of the transmission spectra of WASP-76b, it was possible to detect a number of atmospheric species that had previously been detected in other works [6][22][17] such as FeI, NaI, LiI, KI and MnI. It was also possible to detect features of FeII, TiI and CrI, which have not been reported in previous studies. Other species such as MgI, NiI and CaII, were also searched for, however, it was not possible to detect their spectral features in the transmission spectra of WASP-76b.

Acknowledgements

I would like to thank my supervisor Prof. Neale Gibson for his continued support throughout this project. I am also grateful to the developers of Numpy, Scipy, Matplotlib, iPython and Astropy packages, which were used extensively in this work.

Contents

1	Introduction	4
1.1	History of Exoplanet Discovery	4
1.2	Exoplanet Discovery Methods	4
1.2.1	Radial Velocity Technique	5
1.2.2	Transit Method	5
1.2.3	Geometry of Transits	6
1.3	Transit Spectroscopy	7
1.3.1	High-Resolution Doppler Spectroscopy	8
1.3.2	Rossiter-McLaughlin Effect	8
1.4	Exoplanet Atmospheric Structure and Properties	8
1.4.1	Hot-Jupiters	8
1.4.2	Equilibrium Temperature	9
1.4.3	Scale Height	9
1.4.4	Modelling Planetary Atmospheres	10
1.4.5	Clouds and Hazes	11
1.5	Future Prospects	12
1.6	History of WASP-76b	12
2	Methods	13
2.1	Pre-processing Data	13
2.2	Model Transmission Spectra	14
2.3	Cross Correlation Techniques	16
2.4	Velocity Summation	18
3	Results and Discussion	19
3.1	FeI	19
3.2	NaI	20
3.3	LiI and KI	20
3.4	TiI	22
3.5	MnI	23
3.6	CrI	23
3.7	FeII	23
3.8	MgI, CaII and NiI	24
3.9	Blueshift of Signals	24
3.10	Future Work	24
4	Conclusions	25

Appendices	28
A Peaks from Planetary Orbital vs Systemic Velocity Maps	28
A.1 FeI	28
A.2 NaI	28
A.3 LiI	29
A.4 KI	29
A.5 TiI	30
A.6 MnI	30
A.7 CrI	31
A.8 MgI	31
A.9 CaII	32
A.10 NiI	32
A.11 FeII	33
B Astronomical Constants	33
C Sample Model Transmission Spectra	34

1 Introduction

1.1 History of Exoplanet Discovery

The possibility of exoplanets, planets outside our own solar system, has been pondered by astronomers for centuries. In the eighteenth century, in his *Principia*, Isaac Newton wrote of this idea. “And if the fixed stars are the centres of similar systems, they will all be constructed according to a similar design and subject to the dominion of One.”

Despite the long history of scientists theorising their existence. It was only in 1992 that the first exoplanets were discovered by Wolszezan and Frail (1992) [20]. These first exoplanets were discovered by noticing anomalies in the period of pulsation of the pulsar around which they orbit. Pulsars are rotating neutron stars that emit a regular stream of radio pulses of period in the millisecond to a few seconds range. It was three years later, in 1995, that the first exoplanets were discovered around a main sequence star [13]. Since these early days of exoplanet discovery, over 4300 more exoplanets have been discovered [2].

Exoplanets display a wider range of properties such as mass, radius, orbital distance, temperature and host star type, than planets in our own solar system. For example the equilibrium temperature of planets in our solar system range between 50 and 500K, and have planetary sizes that fall into three main categories - the gas giants ($8-11 R_{\oplus}$, $\sim 100-320 M_{\oplus}$), the ice giants ($4 R_{\oplus}$, $\sim 14-17 M_{\oplus}$), and the terrestrial planets ($\leq 1 R_{\oplus}$, $\leq 1 M_{\oplus}$). Meanwhile the exoplanets discovered so far have equilibrium temperatures ranging 200-4000K, and have radii and masses continuously spanning over the range $\sim 0.5-20 R_{\oplus}$ and $\sim 1-10^4 M_{\oplus}$ [12].

Due to this broader range of planetary properties, the atmospheres of these exoplanets are much more diverse than those present in our solar system. Understanding the atmospheric composition of these exoplanets will help provide an insight into planetary formation and migration mechanisms and geophysical processes. The techniques developed for these atmospheric analyses may also be used in the future for the search of biosignatures and possible signs of alien life.

1.2 Exoplanet Discovery Methods

The majority of stars are located at such large distances, that they cannot be spatially resolved and act as point sources. Due to this, it is not usually possible to directly observe or image any exoplanets orbiting around their host star using direct techniques such as direct imaging or gravitational microlensing.

Exoplanets are therefore usually discovered by studying the effect they have on the light coming from their host star using indirect methods such as the radial velocity technique and the transit method. While exoplanets have been discovered using all the methods mentioned above, the transit method has led to the most discoveries [2].

More than 99% of the exoplanets discovered so far are massive planets, larger than any planet in our Solar System, and orbit close to their host star with a short period. It is important to remember that these discovered exoplanets are only a subset of all the exoplanets out there in space and that this subset is heavily biased due to the detectability factors of the detection methods [11].

1.2.1 Radial Velocity Technique

It is a common misconception that planets orbit around their host star. In fact, both bodies orbit around their common centre of mass, the barycenter. This means that the star wobbles around the barycenter with the same period as the planet. The more massive a planet, or the smaller the planet's orbital radius, the larger the amplitude of the wobble. This periodic motion of the star causes a periodic Doppler shift of the light coming from the star.

The first step in this technique is to measure the velocity at which the barycenter of the system is moving away from Earth. This is achieved by fitting the Doppler shift of the stellar spectrum. Once this velocity is calculated, the stellar spectrum can be shifted to the rest frame of the barycenter. This means that the remaining motion of the star is due to the orbiting exoplanet.

Not all stars with orbiting exoplanets exhibit this effect. The radial velocity technique is dependent on the orientation of the orbital plane of the stellar system. For the radial motion of the star to be measurable, the angle between the orbital plane and the line of sight must be relatively small.

The amplitude of the radial velocity variations, K , of a star of mass M_\star , induced by a planet of mass M_P is given by:

$$K = \left(\frac{2\pi G}{P_{\text{orb}}} \right)^{1/3} \frac{M_P \sin i}{(M_\star + M_P)^{2/3}} \frac{1}{\sqrt{1 - e^2}} \quad (1)$$

where P_{orb} is the orbital period, i is the angle between the normal to the orbital plane and the line of sight, e is the orbit's eccentricity. The value of e ranges from 0 to 1, with the eccentricity of most hot-Jupiter exoplanets such as WASP-76b, being very close to 0 due to their near circular orbits.

The stellar mass can be estimated by analysing the spectral characteristics and measured distance of the star. Using this information and the information from the radial velocity method, the value $M_P \sin i$ can be calculated. The exact mass of the planet M_P cannot be calculated using this technique as the angle i cannot be derived. This means that there is a certain amount of ambiguity associated with this technique as it cannot distinguish between a massive planet with an orbital plane at a large angle to the line of sight and a less massive planet with an orbital plane oriented along the line of sight. Despite its shortcomings, this technique can be very useful when paired with the transit method [11].

1.2.2 Transit Method

The transit method, also called transit photometry, is the most popular method for exoplanet discovery. This method requires the orbital plane of the exoplanet to be near or along the line of sight. As the exoplanet passes in front of the host star, a small amount of light from the star is blocked and the star appears to get dimmer. Using precise measurements of the fluctuations of stellar brightness as a function of time, exoplanet transits can be distinguished by their periodicity and shape, from other intrinsic solar brightness variations such as star spots.

The change in stellar flux, ΔF , over the total flux, F , can give an estimate on the ratio between the radius of the host star to radius of the exoplanet. The relationship is given by:

$$\frac{\Delta F}{F} = \frac{R_P^2}{R_\star^2} \quad (2)$$

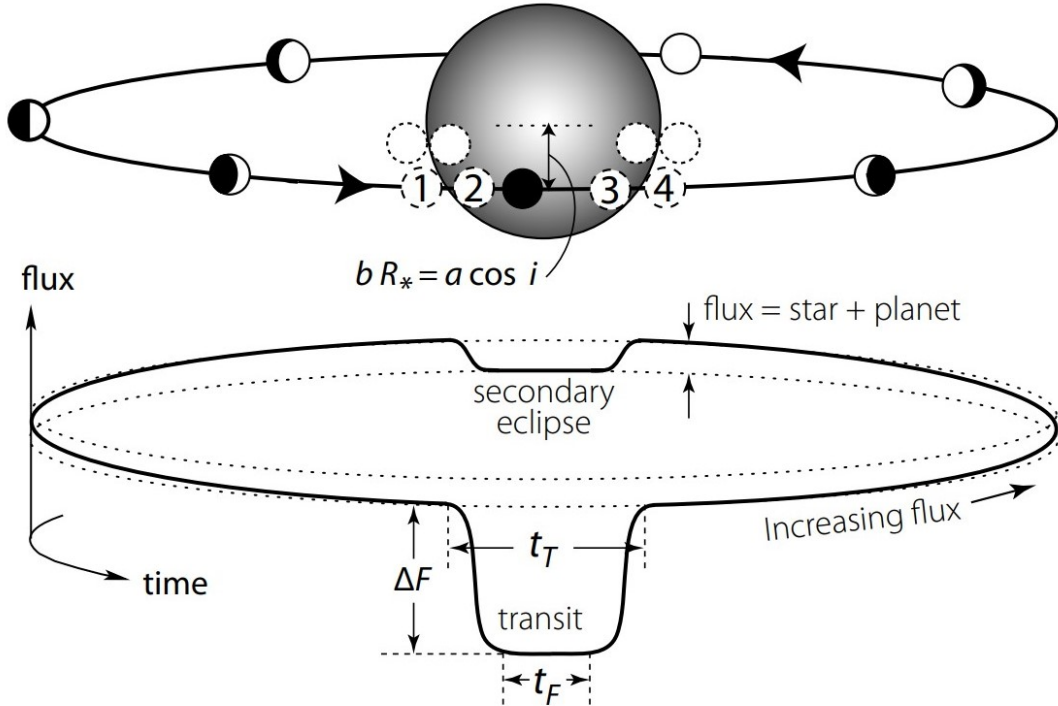


Figure 1: Illustration of the variation in stellar flux as a function of orbital phase for a transiting exoplanet. [14]

where R_P is the radius of the exoplanet and R_* is the radius of the host star. This does not confirm that the change in flux was caused by an orbiting exoplanet, only that there is a Jupiter sized opaque body orbiting the star. To confirm that the body is an exoplanet and not, for example, a brown dwarf star, the mass of the transiting body needs to be found. This can be done using the radial velocity technique [8], as discussed previously.

1.2.3 Geometry of Transits

For the transit of an exoplanet to be observed, the orbit normal must be nearly perpendicular to the line of sight (i.e. $i \approx 90^\circ$). If a planet of radius R_P orbits a star of radius R_* , at a distance of a , the probability of observing a transit of a randomly orientated planet is given by [8]:

$$P_{\text{tr}} = \frac{R_* + R_P}{a} \approx \frac{R_*}{a} \quad (3)$$

This equation shows how the transit method strongly selects for large exoplanets that orbit very closely to their host star. For example, the probability of detecting an exoplanet at the same orbital radius as Jupiter (5.2AU) transiting a solar radius star is approximately 0.09%, while if it orbited at the typical radius of a hot-Jupiter exoplanet (0.05AU) the probability of detection increases to 9%.

Another important geometric factor in transits is the impact parameter, b , which is defined as the shortest distance from the center of the stellar disc to the path of the planet, as shown in figure 1.

When describing the phases of an exoplanet transit, there are four important points or contacts. The first contact is when the limb of the planetary disc first coincides with the stellar disc and the stellar flux

begins to decrease. The stellar flux continues to decrease until the second contact, which is the point where all of the planetary disc is just within the stellar disc. The stellar flux remains constant until the third contact, which is the last point at which the planetary disc is fully within the stellar disc. The stellar flux then rises again until the fourth contact, when the planetary disc is completely passed the stellar disc. These contacts are illustrated in figure 1.

The total transit time, t_T , is defined as the time between the first and fourth contacts. For an exoplanet system with impact parameter $b = 0$, and radii $R_\star \gg R_P$, the total transit time is given by [8]:

$$t_T \approx \frac{PR_\star}{\pi a} \quad (4)$$

From the transit method, the mass and radius of the orbiting exoplanet can be calculated.

1.3 Transit Spectroscopy

Transit spectroscopy is a technique used to infer the atmospheric properties of transiting exoplanets. It allows for three configurations of the planet to be observed, each able to obtain information on different aspects of the planetary atmosphere.

The first configuration is the primary eclipse, obtained as the planet passes in front of the host star. During the primary eclipse, some of the light from the star passes through the atmosphere along the day-night terminator of the planet. The resulting spectrum contains the absorption features of the atmospheric species along with the stellar spectrum. Removing the stellar spectrum leaves behind only the transmission spectrum of the transiting exoplanet. Since the radius of the planet can be determined using the transit method, transit spectroscopy measures the wavelength dependence of this effective planetary radius.

The second configuration is the secondary eclipse, when the planet passes behind its host star. Just before the planet passes behind the star the spectrum contains both the stellar spectrum and the emission spectrum from the exoplanet. By measuring the stellar spectrum on its own during the secondary eclipse, and subtracting it from the total spectrum, the planetary emission spectrum can be obtained.

The final configuration is the phase curve, as the planet orbits between the primary and secondary eclipse. The phase curve provides a spectrum of the planet at different phases throughout its orbit, and is useful for providing constraints on the atmospheric dynamics and energy transport present on the exoplanet. All three configurations are illustrated in figure 1.

This project focuses on the transmission spectra obtained during the primary eclipse of WASP-76b. The transmission spectrum is excellent at providing constraints on the chemical composition of the atmosphere along the day-night terminator. It is also very useful for investigating scattering occurring in the atmosphere. Different types of scattering occur from, different sources, such as a Rayleigh scattering from small particles and Mie scattering from larger particles. The scattering leaves distinct spectral features in the transmission spectra, which can be used to investigate the presence of clouds or hazes in the atmosphere.

1.3.1 High-Resolution Doppler Spectroscopy

High-resolution Doppler spectroscopy is an effective way of detecting the atmospheric composition of close-in giant exoplanets such as hot-Jupiters. Due to the short orbital period of these close-in planets, they travel at high velocities causing a significant Doppler shift in the planetary spectral lines. This Doppler shift is used to separate the transmission spectrum of the planet from the stellar spectrum. The transmission spectra are cross-correlated with model transmission spectra of the expected chemical species. The planet spectrum is then matched with the planetary orbital velocity and systemic velocity. A high significance peak in the orbital and systemic velocity plane implies a detection of the species present in the model spectrum, such as in figure 6. This process is explained in more detail in section 2.3 and 2.4. Typically a peak above 3σ signal-to-noise is considered to be a detection and a peak above 5σ is considered to be a strong detection [12].

High-resolution Doppler spectroscopy is a very effective way of detecting the presence of chemical species in exoplanet atmospheres. However, this method does have certain drawbacks. The detection significances of the species rely greatly on the metrics used to quantify the signals and also the detrending methods used to separate the planetary transmission spectrum from the stellar spectrum. This method also is not excellent at measuring the abundances of the detected species, as the method is more sensitive to the position of the lines rather than their depths. However, this problem can be overcome by pairing this method with low-resolution transmission spectroscopy.

1.3.2 Rossiter-McLaughlin Effect

The Rossiter-McLaughlin effect is a spectroscopic phenomenon observed when an object moves across a star. Due to the rotation of the star, light from different parts of the stellar surface are either blue or redshifted. The light coming from the side of the star that is rotating away from us is redshifted, and the light coming from the side rotating towards us is blueshifted. It is not usually possible to resolve the disc of a star to observe the Doppler shift from each side of the star, however, usually the shift from each side cancel the other out, leading to mean red/blueshift of zero. However, when the transiting exoplanet passes in front of the star it blocks part of the shifted spectra, and the mean redshift will vary from its normal value. It will increase when the planet is in front of the blueshifted part of the star and decrease when it is in front of the redshifted side[8].

The change in mean redshift can indicate spin-orbit angle of the stellar system. The spin orbit angle is the angle between the rotational axis of the star and the orbital axis of the transiting exoplanet. This property can give insight to the star and planet formation history [11].

1.4 Exoplanet Atmospheric Structure and Properties

1.4.1 Hot-Jupiters

Hot-Jupiters are a class of gas giant exoplanets similar in size to Jupiter and with a very short orbital period, usually around 10 days. Due to this short period they orbit quite close to their star, usually around 0.1AU. Most hot-Jupiters have orbits with very low eccentricity, meaning their orbits are nearly

circular. This is due to the fact that eccentric orbits close to the star will be rapidly damped by the tidal forces, which are strongly dependent on radius. The eccentricity of the transiting exoplanet's orbit can be calculated by measuring the difference in duration of the primary and secondary eclipse of its orbit, as illustrated in figure 1 [11].

Many hot-Jupiters are believed to exhibit tidal locking. This means that the spin of the exoplanet is synchronised with the orbit, causing the same side of the planet to be constantly presented to its host star, similar to the way the same side of the Moon always faces Earth.

1.4.2 Equilibrium Temperature

One of the most important parameters characterising an exoplanet is the equilibrium temperature. The equilibrium temperature is defined as the temperature for which the planet is in thermal equilibrium, i.e. the planet radiates the same amount of thermal energy as it receives from its host star. This temperature is given by the equation [8]:

$$T_{\text{eq}} = \left(\frac{(1 - A_{\text{B}})F}{4\sigma} \right)^{1/4} \quad (5)$$

where F is the stellar flux from the host star, A_{B} is the planetary bond albedo, the fraction of intercepted light reflected by the planet and σ is the Stefan-Boltzmann constant. When discussing exoplanets, the equilibrium temperature is often given in terms of the temperature and radius of the host star [14]:

$$T_{\text{eq}} = T_{\star} \left(\frac{R_{\star}}{2a} \right) [f(1 - A_{\text{B}})]^{1/4} \quad (6)$$

where T_{\star} is the effective temperature of the host star, R_{\star} is the stellar radius, a is the planet's semi major axis. The factor f describes the effectiveness of atmospheric circulation and the degree to which energy is transferred from the day side to the night side of the planet. For tidally locked planets, where the incident energy from the star is redistributed all around the planet, giving a uniform equilibrium temperature, $f = 1$. If the day side alone reradiates the energy and the night side remains cold, $f = 2$ [14].

1.4.3 Scale Height

The scale height is a useful concept when modelling and studying planetary atmospheres. It is defined as the height through which the pressure decreases by a factor of $1/e$ [4]. It is derived by assuming that an isothermal atmosphere at temperature T , has a density ρ_0 at the surface and density ρ_h at height h above the surface. Consider a small section of the atmosphere of unit cross-section, at height x and of thickness dx . The forces acting on this section are pressure acting upwards of P , pressure acting downwards of $P + dP$ and weight acting downwards of $\rho_x g dx$, where g is the surface gravity. These lead to the expressions:

$$P + dP + \rho_x g dx + P = 0 \quad (7)$$

$$\frac{dP}{dx} = -g\rho_x \quad (8)$$

Assuming an ideal gas, the pressure can be given by:

$$P = \frac{\rho k T_{\text{eq}}}{\mu} \quad (9)$$

where k is Boltzmann's constant and μ is the mean molecular mass of the atmosphere. Differentiating this expression with respect to x leads to the following expression, which can then be subbed into equation (8) above.

$$\frac{dP}{dx} = \frac{k T_{\text{eq}}}{\mu} \frac{d\rho}{dx} \quad (10)$$

$$\frac{d\rho}{dx} = -\frac{\mu g h}{k T_{\text{eq}}} \quad (11)$$

Integrating the above equation with boundary conditions $x = 0$ and $x = h$ gives:

$$\rho_h = \rho_0 \exp\left(-\frac{\mu g h}{k T_{\text{eq}}}\right) \quad (12)$$

this equation can also be given in terms of pressure as for an isothermal atmosphere, pressure is proportional to density.

$$P_h = P_0 \exp\left(-\frac{\mu g h}{k T_{\text{eq}}}\right) \quad (13)$$

Therefore, the scale height H , which is the value of h which leads to a decrease in pressure of $1/e$, can be given by:

$$H = \frac{k T_{\text{eq}}}{\mu g} \quad (14)$$

The atmospheric scale height is an effective way of describing how the density of the atmosphere changes with altitude. Small values of scale heights imply a rapid decrease in atmospheric pressure with altitude, while large values imply a slower decrease of pressure with altitude.

1.4.4 Modelling Planetary Atmospheres

When trying to detect atmospheric species using high-resolution Doppler spectroscopy, it is necessary to construct models of the planetary atmosphere in order to generate model transmission spectra. This can be done using the equation described in Gibson et al.(2020) [7]. This equation was modified from an equation in a previous paper by Heng and Kitzmann (2017) [9]. It was modified to depend on the cross section per atom $\sigma(\lambda)$ and to include multiple species indexed by j . The equation for the effective radius of the planet is given by:

$$R(\lambda) = R_0 + H \left[\gamma + \ln \left(\frac{P_0}{\mu g} \sqrt{\frac{2\pi R_0}{H}} \right) \right] + H \ln \sum_j \chi_j \sigma_j(\lambda) \quad (15)$$

where H , g and μ are the scale height, surface gravity and mean molecular mass of the atmosphere. R_0 and P_0 are the reference radius and pressure and γ is a dimensionless constant. χ_j is the volume mixing ratio of the species under consideration. When using the equation above, it is necessary to calculate the surface gravity, g , of the planet being studied. This can be done using the following expression:

$$g = \frac{GM}{R^2} \quad (16)$$

where G is the gravitational constant, M is the mass of the planet and R is the radius of the planet. This can then be used to calculate the scale height H of the atmosphere.

1.4.5 Clouds and Hazes

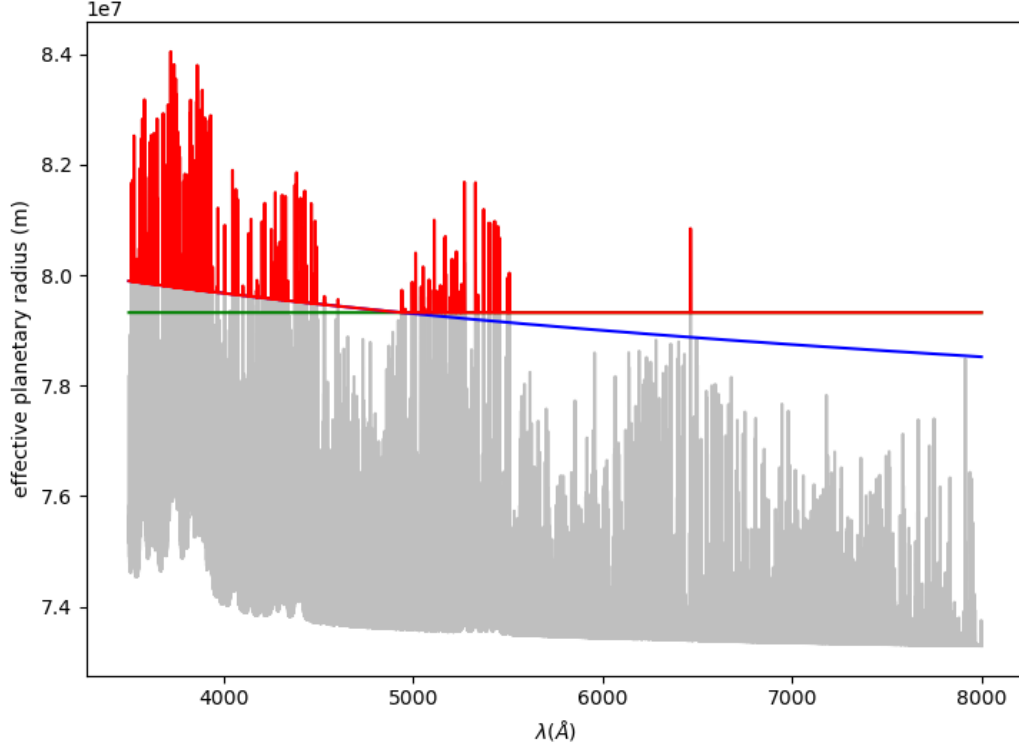


Figure 2: Sample spectrum for neutral iron at an atmospheric temperature of 2500K. The green line shows the truncation due to the cloud deck and the blue line is caused by Rayleigh scattering.

Condensates, an umbrella term for clouds and hazes, are found in almost all of the atmospheres of planets in our solar system and there is a growing body of evidence suggesting that they are common in hot-Jupiter exoplanets, with approximately half of the spectroscopically analysed hot-Jupiters displaying evidence of condensates in their spectra [16].

Clouds and hazes effect the spectra of exoplanets in three ways. Firstly, they completely block transmission of stellar flux, effectively truncating the spectral features below the cloud-deck height [10]. Secondly, they introduce a slope in the spectrum over wavelength intervals of several microns. This slope is dominated by Rayleigh scattering effects [16]. The third effect is a steep increase in transit depth towards the blue end of the spectrum caused by scattering off condensate particles at optical wavelengths. This is due to the condensate particles efficiently scattering radiation with wavelengths comparable to the size of the particles [15]. Figure 2 illustrates the effect of a cloud deck on the spectrum of neutral iron in the planetary atmosphere.

The exact chemical composition of clouds and hazes is currently unknown as current transmission spectra lack the wavelength coverage and precision needed to distinguish between the possible species. However, there are a few possibilities that are theorised such as equilibrium condensates like water, salt, sulfide or silicate clouds and photo-chemical hazes such as hydrocarbon soot formed from photolyzed

methane [10].

The altitude of the cloud deck is dependant on the pressure and temperature of the atmosphere, and the chemical composition of the cloud deck. In this project, the cloud deck was calculated for various temperatures and pressures.

1.5 Future Prospects

This is a very exciting time for atmospheric research of exoplanets, with many new discoveries being made. Over the coming years there are numerous new observing facilities being established. Some of the most important of these facilities include the Transiting Exoplanet Survey Satellite (TESS), launched in April 2018, which is expected to discover thousands of transiting exoplanets, including small exoplanets less than four Earth radii. Another important upcoming instrument is the James Webb Space Telescope (JWST), set to launch in October 2021. The JWST is to replace the Hubble Space Telescope as NASA's flagship telescope.

These telescopes have greater aperture size and wavelength coverage than current instruments, which are the main technical limitations on atmospheric characterisation. With these new instruments, it is hoped that it will be possible to use transmission spectroscopy techniques on much smaller exoplanets, including Earth size terrestrial planets, with the possibility of searching for biosignatures in these exoplanet atmospheres.

1.6 History of WASP-76b

WASP-76b was first discovered using a combination of the transit and radial velocity method by West et al.(2013) with the SOPHIE and CORALIE spectrographs and the TRAPPIST photometer [19]. Using the methods given by Doyle et al.(2013) [5], the stellar parameters of the host star WASP-76 were derived. WASP-76 is an F7, 0.95 magnitude, main sequence star with a mass of $1.46M_{\odot}$. It has a rotation rate of $P = 17.6 \pm 4.0$ days which gives the star a gyrochronological age of approximately 5.3Gyr. It is located 120 ± 20 pc away from Earth in the direction: RA= $01^{\text{h}}46^{\text{m}}31.86^{\text{s}}$, Dec= $+02^{\circ}42'02.0''$. It was also discovered that WASP-76b has an inflated radius ($1.83R_{\text{Jup}}$), meaning it is a bloated hot-Jupiter. This is likely caused by the high temperature and large radius of its host star. The planet orbits with a nearly circular path with an eccentricity of 0.05, with a period of 1.81 days. The mass of the exoplanet is $0.92M_{\text{Jup}}$ [19].

A number of papers have also begun the atmospheric characterisation of WASP-76b. From archival data of previous planet searching surveys, the spectroscopic time series were analysed and strong signals of NaI were detected with a detection significance of 7σ by Zak et al.(2019) [22]. More recent observations of WASP-76b by Tabernero et al.(2020) have confirmed this finding and have also found signs of other atmospheric species such as LiI, MgI, CaII, MnII, KI and FeI [17].

Ehrenreich et al.(2020) discovered that there is evidence to suggest that the atomic iron in the atmosphere of WASP-76b condenses during its journey across the night side of WASP-76b [6]. This was discovered by the detection of an asymmetric absorption signal from neutral iron present on the evening

terminator but not on the morning terminator of the planet. This paper also found evidence of strong winds in the planetary atmosphere blowing from the hot day side to the cooler night side. This wind was found by a strong blueshift of absorption signals on the limbs of the exoplanet.

2 Methods

2.1 Pre-processing Data

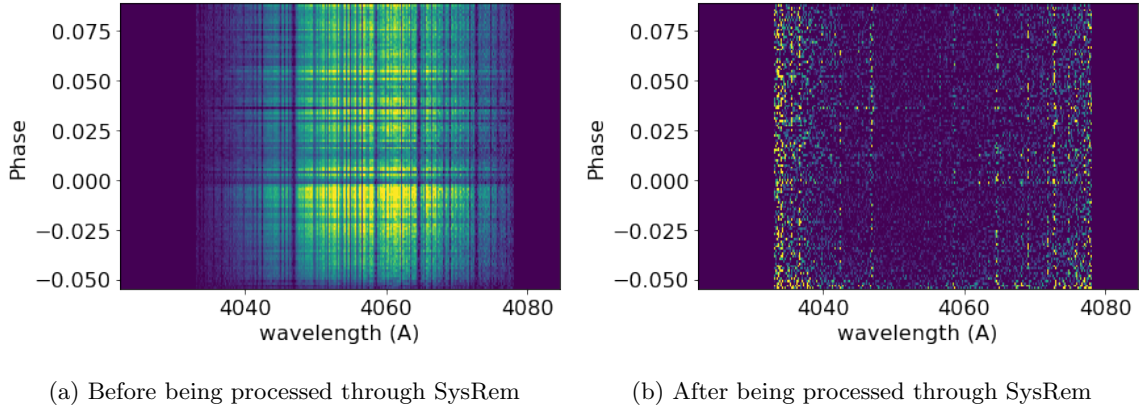


Figure 3: Tenth order spectra after paired orders being combined. Figure 3a shows the spectrum after being blaze corrected and shifted to the stellar rest frame. Figure 3b shows the spectrum after being processed through SysRem for 15 iterations to remove the stellar and telluric signals

The time-series spectroscopy of one transit of WASP-76b was observed using the ESPRESSO instrument at the VLT. 117 high-resolution echelle spectra were collected using the 1UT HR mode of ESPRESSO. The spectra covered the optical wavelengths from 3800 to 7880Å. The spectra were observed with an exposure time of 150 seconds with a readout time of 44 seconds, resulting in a cadence of 194 seconds. The spectra from the observations were provided by Prof Neale Gibson. Each spectrum was in the form of a 3D data cube subdivided into 170 orders. The spectra were provided preprocessed, having been cleaned and blaze corrected, and shifted to the stellar rest frame. Due to the set up of ESPRESSO, each order was observed twice. To reduce the volume of the data, the paired orders were combined. This was done by interpolating the second order to the first and taking a weighted average. This halved the number of orders, bringing it to 85 orders per spectrum.

The next step in processing the data was to remove the stellar and telluric signals from the spectra. Telluric signals are signals that originate from the Earth’s atmosphere that contaminate spectra. As targets move across the sky, the seeing conditions such as airmass, water vapour and cloud cover vary. This leads to changes in the light curve that can sometimes be orders of magnitude larger than the planetary signal [10].

Early methods for removing these signals was to remove any signal that remains at a constant wavelength throughout the time of the observation. This can be done by dividing the spectra by their mean. Since the spectra are in the stellar rest frame, the stellar signals do not change with time, while the

planetary signal, which moves relative to the stellar rest frame does. While this method works for removing stellar signals, it is not effective at removing telluric signals, due to the transparency of Earth’s atmosphere changing with time.

It is more effective to implement a machine learning algorithm such as SysRem to remove the stellar and telluric signals. SysRem is a detrending algorithm designed to remove systemic effects in large sets of light curves from photometric surveys [18]. It can remove effects such as atmospheric extinction, detector efficiency and point spread function changes over the detector. One of the big advantages of this algorithm is that it does not require prior knowledge of the effects to remove them.

The SysRem algorithm was applied in a similar way as Gibson et al. (2020) [7]. SysRem was applied for 15 iterations on each order’s spectrum and the uncertainty in the spectrum, to construct a model of the data. The original data set was then divided by the absolute value of the SysRem model before subtracting one. The uncertainties were also divided through by the same SysRem model. This method preserves the relative depths of the planet’s transmission spectra, while allowing the raw measured flux to be modelled directly. Figure 3 shows the spectrum from the tenth order before and after it had been processed using the SysRem algorithm.

Previous studies have indicated that the filtering of data with algorithms such as SysRem can alter the planetary signal embedded in the data, however it has been found that these methods do not significantly impact the extracted values [7]. Removing stellar and telluric signals from planetary atmospheric signals is one of the biggest challenges in using high resolution techniques to probe exoplanetary atmospheres.

2.2 Model Transmission Spectra

In order to search for the features of chemical species in the transmission spectrum of WASP-76b using high resolution cross-correlation techniques, it is first required to generate models of the planetary atmosphere to create cross-correlation templates. The atmospheric cross-sections for a large number of species were provided by Prof. Gibson, calculated for a large range of temperatures. These cross-sections were then used to compute the model templates for WASP-76b. This was done using equation 15, described in section 1.4.4.

The dimensionless constant was taken to be $\gamma = 0.54$ and the volume mixing ratio of the species under consideration was taken to be $\chi_j = 1 \times 10^{-7}$. These quantities were derived from other planetary parameters, which were taken from previous work on WASP-76b by Ehrenreich et al. (2020) [6]. The mass and radius of the planet were taken to be $R = 0.10852R_\odot$ and $M = 0.894M_{\text{Jup}}$. The stellar radius of WASP-76 was taken to be $R_\star = 1.756R_\odot$. The mean molecular weight was fixed to be $\mu = 2.3m_p$. Using these values, the surface gravity of WASP-76b was calculated as described before.

Using this value for g , the scale height for the atmosphere could be calculated using equation (6) as discussed in section 1.4.3. The atmospheric temperature was fixed to be $T = 2300\text{K}$ for this calculation. Due to the degeneracy between reference pressure, radius and abundance [9], it is not necessary to vary all these parameters when generating new atmospheric templates, as it is possible to obtain identical templates using different combinations of abundance and reference radius. Therefore it was possible to fix the abundance and vary the temperature and cloud deck pressure.

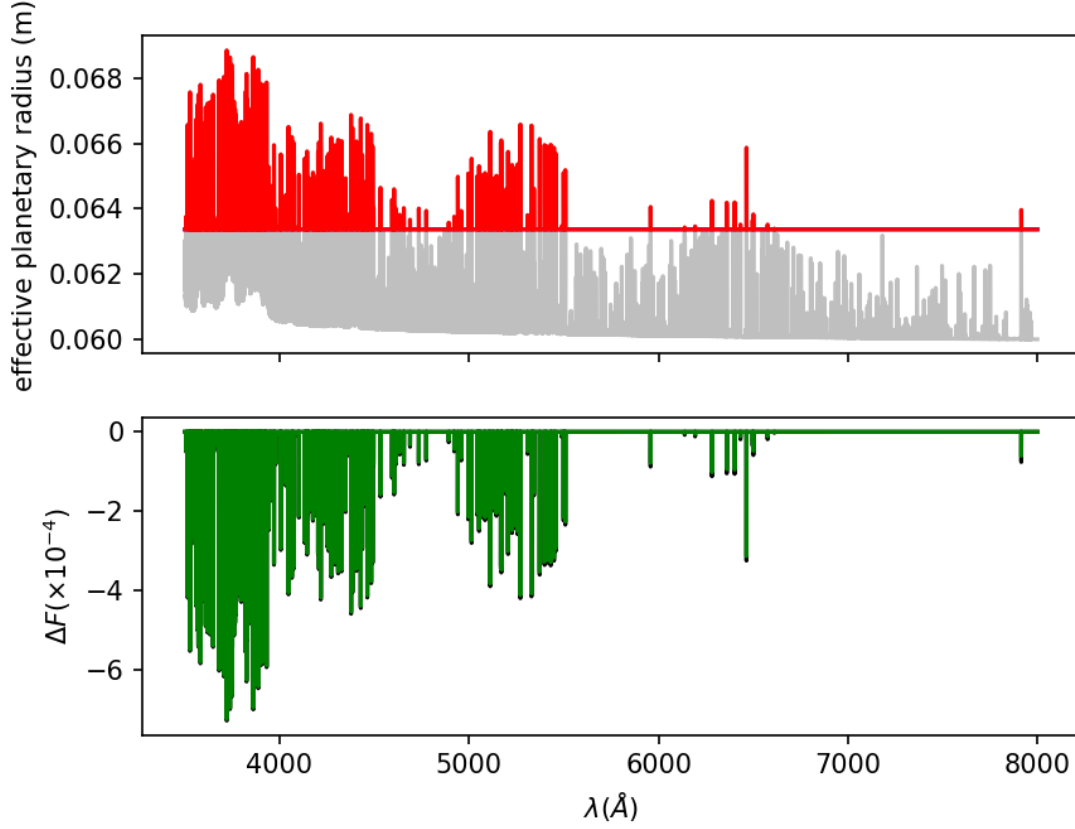


Figure 4: Model transmission spectra for FeI at a temperature of 2000K with a cloud deck located at an altitude with an atmospheric pressure of 1×10^{-1} bar. The first figure is in terms of effective planetary radius (m) and it can be seen how the cloud deck truncates the model transmission. The second figure is given in terms of change in stellar flux, ΔF and is the model spectrum used in the cross-correlation techniques.

In order to use these templates for high resolution transmission spectroscopy, they are required to be in units of negative delta flux $-\Delta F$. This was done by subtracting the square of the radius of the continuum from the square of the radius calculated using equation (7).

Once the transmission spectra had been calculated and truncated by the cloud deck, the model transmission spectra were broadened slightly by convolution using a Gaussian kernel. This was done to simulate the broadening of spectral lines in real data from sources such as rotation and instrumental broadening.

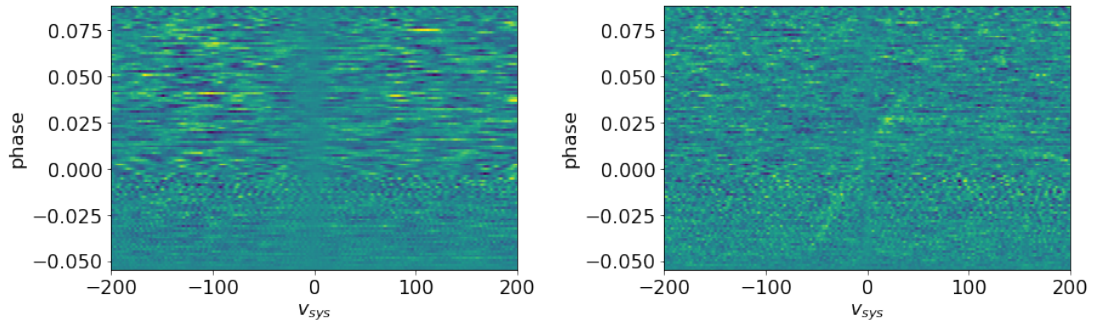
Figure 4 gives an example of a model transmission spectrum. In the first figure, the grey line illustrates the full transmission spectrum for FeI at an atmospheric temperature of 2000K, while the red shows the spectrum after it has been truncated by the cloud deck. The second figure shows the same model transmission spectrum but given in terms of ΔF .

This procedure was used to create model transmission spectra for a number of atmospheric species to be used for the cross-correlation techniques. The species for which models were created were FeI, NaI,

LiI, MgI, CaII, MnI, KI, TI, CrI and NiI. Each species had models generated at four atmospheric temperatures, 2000K, 3000K, 3500K and 4000K. At each temperature, a spectral model was calculated for six different cloud deck altitudes located at the atmospheric pressures, 1×10^{-1} , 1×10^{-2} , 1×10^{-3} , 1×10^{-4} , 1×10^{-5} , and 1×10^{-6} bar. Separate model transmission spectra were generated for FeII, as due to the shape of its spectra, the cloud deck pressures used for the model transmission spectra of the other species were too low. Using these pressures resulted in a cloud deck that was much higher than the features of the transmission spectra, completely obscuring it. Therefore, separate values of pressure were used. For each atmospheric temperature, a spectral model of FeII was calculated for six different cloud deck altitudes located at the atmospheric pressures, 1000×10^{-1} , 1000×10^{-2} , 1000×10^{-3} , 1000×10^{-4} , 1000×10^{-5} , and 1000×10^{-6} bar.

Appendix C contains a sample of the model transmission spectra made for each atmospheric species, all with a temperature of 2000K and a cloud deck at a pressure of 1×10^{-1} bar, apart from FeII, which has a cloud deck at a pressure of 1000×10^{-1} bar.

2.3 Cross Correlation Techniques



(a) CCF map of the 10th order after applying the CCF for a range of systemic velocities v_{sys} . (b) Final CCF map after summing over all orders of the spectra

Figure 5: The above CCF maps were generated with a model transmission spectrum of FeI with an atmospheric temperature of 3000K and a cloud deck located at an atmospheric pressure of 1×10^{-1} bar. The signal from the planetary transit of WASP-76b cannot be seen in figure 5a, but can be seen after summing over all the orders in figure 5b

In signal processing, the correlation operation is similar to convolution. It involves sliding one function over another, multiplying the two together and finding the area under the resulting function. It differs from convolution as there is no ‘folding’ of the function. The maximum of the correlation is obtained when the functions overlap the most. When correlation is carried out using two identical functions it is referred to as autocorrelation. When it is carried out using two different functions it is referred to as cross-correlation. The cross-correlation, $r_{xy}(t)$ of two functions $x(t)$ and $y(t)$ is given by [1]:

$$r_{xy}(t) = x(t) \star y(t) = \int_{-\infty}^{\infty} x(\lambda)y(\lambda - t)d\lambda \quad (17)$$

The term t , is the offset of the the two functions and varying this is what ‘slides’ one function over the

other. It is often referred to as the lag.

Cross-correlation functions (CCFs), such as the one described above, are used in high resolution transmission spectroscopy to match observations with model transmission spectra, such as those generated in section 2.2. This is because the individual lines in transmission spectra are too faint to be observed directly. CCFs sum over many spectral lines, allowing the signal to be boosted.

While there is already a fast cross-correlation function built into the Numpy Python package, this cannot be used for exoplanetary observations. This is due to the way in which Numpy implements the cross-correlation function. Numpy computes the CCF by linearly shifting the function by 1 pixel for each time step. However, astronomical spectra are shifted by the Doppler effect which does not result in linear shifts in wavelength. The relativistic Doppler effect is given by [21]:

$$\lambda = \lambda_0 \sqrt{\frac{1 + v/c}{1 - v/c}} \quad (18)$$

where v is the radial component of the velocity, c is the speed of light, λ is the observed wavelength and λ_0 is the rest wavelength. However, since the velocities are relatively low this can be simplified to:

$$\lambda = \lambda_0 \left(1 + \frac{v}{c}\right) \quad (19)$$

Due to the nonlinear shifting of spectra, a new cross-correlation function had to be generated to account for this. This was done by creating Doppler shifted versions of the model transmission spectra generated in section 2.2. Firstly, a range of systemic velocities (v_{sys}) which are equivalent to the lags was created. The value of velocity ranged from -200 to 200km/s in steps of 0.2km/s . For each value of velocity, the wavelengths of the model transmission spectra were shifted using equation (11) to create an array of shifted wavelengths. These shifted wavelengths could then be used to interpolate the values of ΔF of the model transmission spectra to the new shifted wavelengths.

The next step was to calculate the CCF of each shifted model spectrum with each order of the SysRem processed observational spectra. This was done by taking the observational spectra and dividing them by the variance, which was obtained by squaring the uncertainties obtained from the SysRem processed data. The CCFs were then calculated by taking the dot product of the observed spectra divided by their variance and the transposed array containing the Doppler shifted model transmission spectra. These CCFs could then be displayed on a systemic velocity vs orbital phase plot such as in figure 5.

The CCFs were then summed up over each order to create a final CCF map. After summing over each order, the planetary signal from the transit can be identified. Figure 5 shows the CCF maps for a single order and after summing over all the orders. These maps were generated with a model transmission spectrum of FeI with an atmospheric temperature of 3000K and a cloud deck located at an atmospheric pressure of $1 \times 10^{-1}\text{bar}$. Looking at the CCF map of a single order, such as in figure 5a, it is impossible to make out the transit of WASP-76b, however after summing over all the orders, a faint signal can be identified by the diagonal line. For other species with weaker signals in the planetary atmosphere, this diagonal line may not be visible and further analysis is required to confirm its presence. This is discussed in section 2.4.

2.4 Velocity Summation

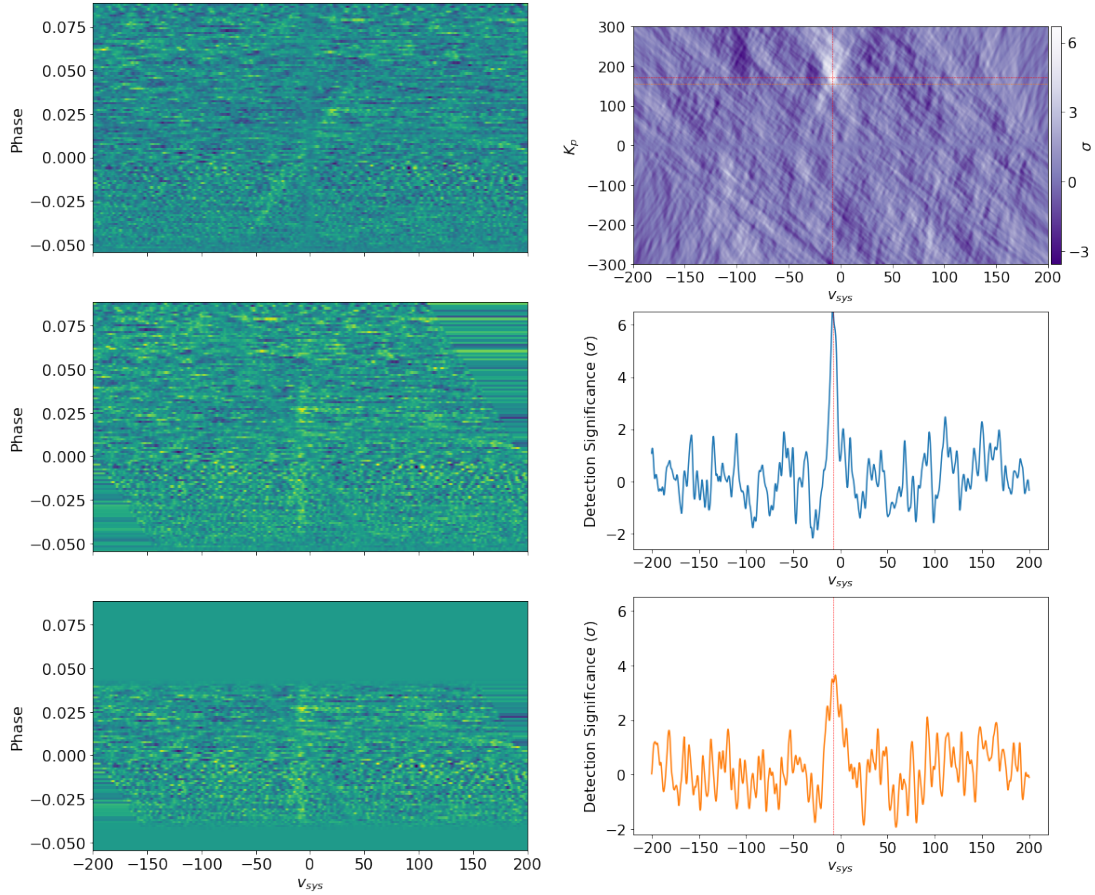


Figure 6: The plots on the left are the CCF map summed over all orders, made with a model transmission spectrum of FeI with an atmospheric temperature of 3000K and a cloud deck located at an atmospheric pressure of 1×10^{-1} bar. They depict the map before and after being shifted to the planet's rest frame, and after being weighted according to the transit function. On the right, the top plot shows the planetary orbital velocity vs systemic velocity map, showing the peak caused by the signal. The second plot is a horizontal slice taken from the peak value of K_p and another horizontal slice taken slightly offset from the peak value of K_p .

In figure 5b, the faint trail of the FeI signal can be seen. However, very often in Doppler shifted spectroscopy, the trail of the planetary signal is too faint to be seen, even after summing over all orders. Hence, further analysis is required to boost the signal. This is done by summing over the velocity trail of the planet. In order to do this, it is necessary to shift the dataset to the planet's rest frame. However, the exact planetary orbital velocity (K_p) is not known and therefore, this must be done for a range of K_p to find the value that gives the best result.

To begin with, an array of values of K_p must be created. The array ranged from -300 to 300 km/s in steps of 0.6 km/s. For each value of K_p , the planet's velocity as a function of phase was calculated using

the equation:

$$v_p = K_p \sin(2\pi\phi) \quad (20)$$

where v_p is the planet’s velocity, and ϕ is the planet’s phase, which was one of the values provided in the observational data. This equation approximates the planet’s orbit to be circular, which is a reasonable approximation for hot Jupiters. These values of planetary velocity were looped over and the values in the CCF map interpolated to the planet’s rest frame for each assumed value of K_p . The shifted CCF maps were then weighted by the transit function so as to only include the data from when the planet was transiting the host star. This process shifts the diagonal transit signal to a vertical one. Figure 6 illustrates a CCF map getting shifted to the rest frame of the planet and then being weighted according to the transit function. The next step is to vertically sum the shifted CCF map. This should lead to a peak being present in the centre of the map. Summing over an incorrect value of K_p may still give a peak, although it will be broader and of lower amplitude. Figure 6 depicts how taking a value of K_p slightly off from the true value results in a lower but broader detection peak.

The velocity summed CCF maps for each value of planetary orbital velocity can now be collated into a orbital velocity vs systemic velocity map. An example of this can be seen in figure 6. This map must be further manipulated in order to give the value of the peak in terms of detection significance, (σ). This was done with a very similar method to the one described in Gibson et al.(2019) [7]. Sections of the map were selected with values of K_p of 150 to 250km/s and v_{sys} of -120 to -60 km/s and 60 to 120 km/s i.e. regions to the left and to the right of the peak. The mean of these regions was calculated along with the standard deviation. The mean was then subtracted from the total map and then divided by the calculated standard deviation. This returns the map in terms of a detection significance, although it is important to note that the exact detection significance will vary slightly with the arbitrarily chosen noise regions. Figure 6 illustrates the final planetary orbital velocity vs systemic velocity map in terms of detection significance.

3 Results and Discussion

3.1 FeI

Neutral atomic iron, FeI, was the first atmospheric species that was searched for in the transmission spectra of WASP-76b, since its detection is well documented in literature [6][17]. This allowed the procedure to be tested to ensure that it was able to make detections with reasonable detection significance.

Using the cross correlation technique with the various atmospheric transmission models generated earlier, a strong detection of FeI was able to be obtained. The peaks with values of systemic velocity, v_{sys} , that were not close to zero were discarded and peaks with unlikely values of planetary orbital velocity, K_p , for example those with negative values, were also discarded. Figure 8 illustrates systemic vs orbital velocity maps with unlikely peak positions.

The remaining peaks were all located in approximately the same location, with a value of $K_p = 172$ km/s and $v_{sys} = -8$ km/s. The model transmission spectrum that generated the largest detection

Table 1: Maximum detection significance obtained for each atmospheric species, details of the model template used and the corresponding values of planetary orbital velocity and systemic velocity.

Species	Temperature (K)	Cloud Pressure (bar)	K_p (km/s)	v_{sys} (km/s)	σ
FeI	3000	1×10^{-1}	173	-8	8.9
NaI	2000	1×10^{-3}	194	-4	7.6
LiI	2000	1×10^{-6}	123	-6	5.8
KI	2000	1×10^{-4}	212	-12	6.0
TiI	4000	1×10^{-1}	212	-8	4.6
MnI	3000	1×10^{-1}	224	-16	6.4
CrI	3000	1×10^{-1}	194	-13	6.0
FeII	4000	1×10^{-6}	227	-2	6.0
MgI	No Detection	-	-	-	-
NiI	No Detection	-	-	-	-
CaII	No Detection	-	-	-	-

significance had an atmospheric temperature of 3000K and a cloud deck located at an atmospheric pressure of 1×10^{-1} bar. It had a detection significance of 8.9σ .

This detection confirms the previous detections in works such as Eihrenreich et al.(2020) [6] and Tabernero et al.(2020) [17]. These works also had very high detection significance, with Tabernero et al.(2020) obtaining obtaining 6.7σ [17].

3.2 NaI

NaI was one of the first species to be identified in the atmosphere of WASP-76b, being detected by Zak et al.(2019) at $7 - 9\sigma$, using archival transmission data from HARPS [22]. NaI was also discovered in other works such as Tabernero et al.(2020) at 7σ [17].

This work was able to make a detection of NaI with a detection significance of 7.6σ . After the maps with peaks in improbable values of K_p and v_{sys} were discarded, the remaining peaks were closely clustered with similar values of K_p and v_{sys} . The model transmission spectrum which obtained the largest detection had a temperature of 2000K and a cloud deck at a pressure of 1×10^{-3} bar. This model's peak was located at $K_p = 194\text{km/s}$ and $v_{sys} = -4\text{km/s}$.

3.3 LiI and KI

It was possible to obtain a detection for LiI from the planet orbital velocity vs systemic velocity maps. However, once the peaks with unphysical values of K_p and v_{sys} were removed, the remaining peaks could be separated into two groups, those with high values of K_p and v_{sys} , and those with lower values. Maps generated with lower temperatures and lower cloud deck pressures created peaks that had mean values of $K_p = 115\text{km/s}$ and $v_{sys} = -4\text{km/s}$. Meanwhile, maps generated with hotter temperatures and

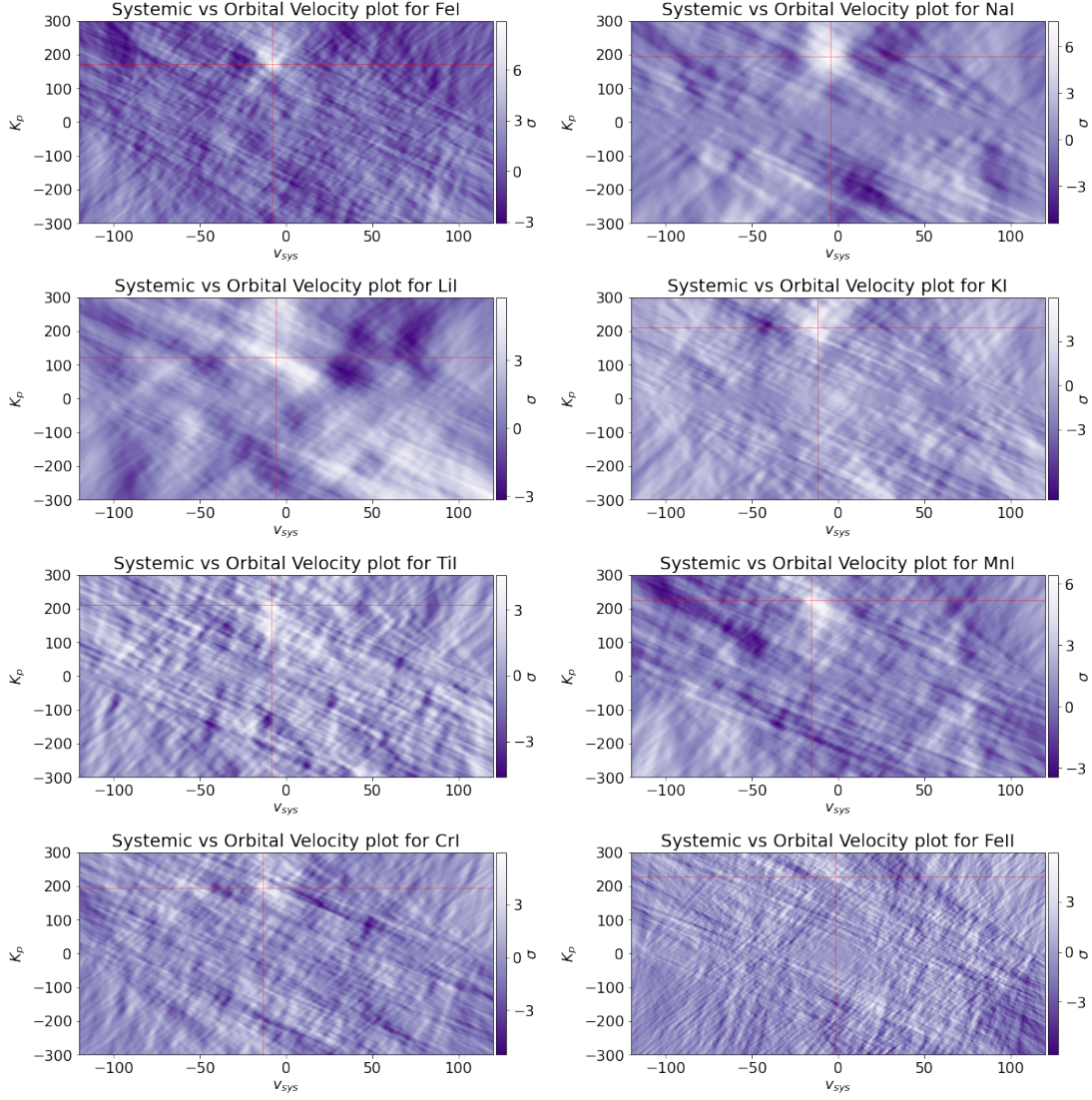


Figure 7: Systemic velocity vs planet orbital velocity maps that obtained the largest detection peak for each chemical species.

higher cloud deck pressures created peaks that had mean values of $K_p = 260\text{km/s}$ and $v_{sys} = -13\text{km/s}$. Both groups of peaks obtained very similar detection significances, with the largest being 5.8σ , obtained from the model with a temperature of 2000K and cloud deck pressure at 1×10^{-6} .

The detection of KI obtained very similar results. After the unphysical peaks were removed, the remaining peaks could also be separated into two groups, however, this time the separation was mainly obtained between models with different cloud deck pressures rather than different atmospheric temperatures. The higher pressure peaks had a higher value planetary orbital velocity with a mean value of $K_p = 214\text{km/s}$, as opposed to the lower pressure peaks having a mean value of $K_p = 179\text{km/s}$. There was not a significant difference between the values of v_{sys} between the two groups. The highest detection significance obtained was 6.0σ and was obtained using the model with a temperature of 2000K and cloud deck pressure at $1 \times 10^{-4}\text{bar}$.

While it is normal for there to be a larger spread in the planetary orbital velocity than in the systemic

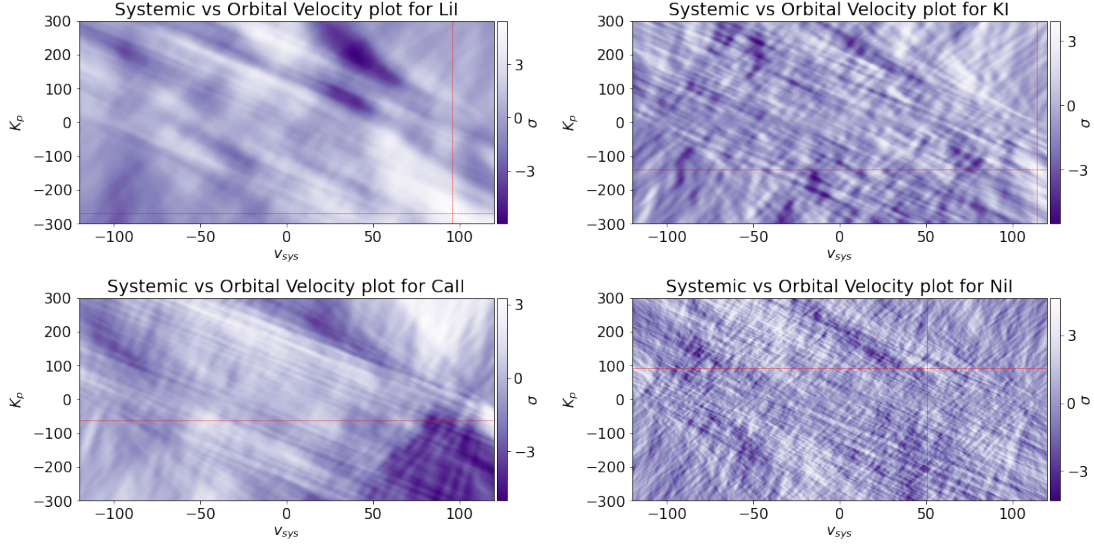


Figure 8: Sample systemic vs orbital velocity maps, with unphysical peak values.

velocity due to the fact that it is more difficult to constrain, the spread obtained for these species, especially LiI, is on the extreme end. One possible reason for such a large spread is that the transmission spectra of these species have a small number of strong lines, causing the velocities to be more poorly constrained.

These detections agree with previous observational work on the atmospheric composition WASP-76b, such as Tabernero et al.(2020) [17]. The presence of LiI also agrees with theoretical atmospheric models such as Baraffe et al.(2015) [3], which state that substellar objects with masses below $\approx 5.5M_{\text{Jup}}$ do not deplete LiI during their evolution. The detection significance obtained from both species were very similar, with LiI having mean of 5.4σ and KI having 4.9σ . This indicates that KI and LiI have very similar atmospheric abundances in WASP-76b. This result was also obtained by Tabernero et al.(2020) [17] who discussed that this finding was unusual as it requires scenarios that have not yet been explored in exoplanetary atmospheres. Some of the possible scenarios suggested in their paper are lithium production taking place in the exoplanet or a strongly inhomogeneous distribution of the species' abundances in the atmosphere of WASP-76b.

3.4 TiI

It was possible to obtain a faint detection of TiI from the transmission spectra of WASP-76b. However, there is reason to be very sceptical of this result. The majority of the model transmission spectra generated peaks with unlikely orbital and systemic velocities and were discarded. Of the few peaks that remained there was a large spread in both the values of K_p and v_{sys} , with K_p ranging from 118 to 212km/s and v_{sys} ranging from -8 to +1km/s. The largest detection significance was 4.6σ , which was obtained using the model with a temperature of 4000K and cloud deck pressure at 1×10^{-1} bar, and had values of $K_p = 212\text{km/s}$ and $v_{\text{sys}} = -8\text{km/s}$.

Another reason to be sceptical about this result is that it disagrees with previous work by Tabernero et al.(2020) [17] which also searched for TiI in the atmosphere of WASP-76b using cross correlation

techniques but was unable to confirm its presence. Further work is required to test the reality of this signal.

3.5 MnI

MnI appears to be in the transmission spectra with a maximum detection significance of 6.4σ . This result was obtained using the model transmission spectra with a temperature of 3000K and cloud deck pressure of 1×10^{-1} bar, and had values of $K_p = 224\text{km/s}$ and $v_{sys} = -16\text{km/s}$.

This result agrees with previous work by Tabernero et al.(2020) [17], which also found MnI to be present in the transmission spectra of WASP-76b.

3.6 CrI

It was possible to detect the presence of CrI in the transmission spectra of WASP-76b. After the peaks with unphysical values of orbital and systemic velocity were removed, there remained a number of peaks, with a large spread in the values of orbital and systemic velocities. The values of K_p ranged from 188 to 258km/s, and v_{sys} ranged from -14 to 7km/s. The largest peak obtained was 6.0σ , which was obtained using the model with a temperature of 4000K and cloud deck pressure at 1×10^{-1} bar, and had values of $K_p = 194\text{km/s}$ and $v_{sys} = -13\text{km/s}$.

The peaks could be separated into two groups. The peaks obtained with larger planetary orbital velocities had lower detection significances than those with lower orbital velocities. This lower detection significance and extreme values of K_p is reason to be sceptical of the peaks obtained at very large orbital velocities.

To the best of our knowledge, this appears to be the first reported detection of CrI in the atmosphere of WASP-76b.

3.7 FeII

The search for FeII in the atmosphere of WASP-76b required special model transmission spectra to be made. Due to the nature of its spectra, the cloud deck pressures used for the model transmission spectra of the other species were too low. Using these pressures resulted in a cloud deck that was much higher than the features of the transmission spectra, completely obscuring it. Due to this, separate values of pressure were used. Therefore, for each atmospheric temperature, a spectral model of FeII was calculated for six different cloud deck altitudes located at the atmospheric pressures, 1000×10^{-1} , 1000×10^{-2} , 1000×10^{-4} , 1000×10^{-4} , 1000×10^{-5} , and 1000×10^{-6} bar.

After analysing the spectra using the cross-correlation techniques as for the previous species, and removing the peaks with unlikely values of orbital and systemic velocities, only two peaks remained. Both of these peaks were had the same values of $K_p = 228\text{km/s}$ and $v_{sys} = -2\text{km/s}$. The highest detection significance of the peaks was 5.9σ . Due to the high value of K_p and the few number of reasonable peaks, there is reason to be sceptical of this detection.

3.8 MgI, CaII and NiI

The presence of MgI, CaII and NiI was explored in the observational transmission spectra, however this was unsuccessful and there was no trace of any of these atmospheric species in the transmission spectra. The lack of NiI was expected, as previous work by Tabernero et al.(2020) [17] was also unable to find any trace of it in the atmosphere of WASP-76b, and was only able to calculate an upper limit of its presence of ~ 130 parts per million.

Previous investigation into the atmospheric composition of WASP-76b by Tabernero et al.(2020) obtained detections for MgI and CaII. They obtained quite low detection significance for MgI from their transmission spectra, at only $2.8 - 3.7\sigma$.

The lack of detection of CaII was surprising as the previous work by Tabernero et al.(2020) found this with a very high detection significance of 8.5σ . They stated that the the CaII H and K lines were some of the most prominent features in the transmission spectrum of WASP-76b. Although they stated that the source of the CaII lines could originate from photo-ionisation at high altitudes, in the upper part of the highly irradiated planetary exosphere. Perhaps searching for CaII using other model transmission spectra, tailored for searching at these higher altitudes could lead to a detection.

The lack of detection for these species implies that they may not be present in the atmosphere of WASP-76b, or that their intensity is well below the minimum noise level of the observations.

3.9 Blueshift of Signals

It was found that despite the CCF maps being shifted to the rest frame of the planet, the peaks did not lie at $v_{sys} = 0\text{km/s}$. All the peaks were blueshifted with respect to the rest frame. This blueshift ranged from -2km/s to -16km/s , depending on the species. These blueshifts are likely caused by winds in the exoplanetary atmosphere, which are frequently reported in literature [6][17][7].

Previous work by Tabernero et al.(2020) [17] and Ehrenreich et al.(2020) [6] also found evidence of winds in the atmosphere of WASP-76b. Due to the high day-side temperature of WASP-76b compared to its night-side temperature, there is theorised to be strong winds blowing from the day-side to the night-side of the planet. However, it is important to note that ultra hot gas giants such as WASP-76b are still an emerging class of exoplanets, and there is not yet a consistent picture of the extreme climates that these exoplanets possess. Current interpretations of wind measurements are based on global circulation models created for less irradiated hot gas giants, and therefore, are not well adapted for objects such as WASP-76b[6].

3.10 Future Work

Due to the limited time frame of this project, there were certain aspects of the analysis of the atmospheric composition of WASP-76b which were unable to be carried out. Given more time it would be possible to gain further insight into the atmosphere of WASP-76b.

One of these aspects would be to investigate the uncertainty in the planetary orbital velocity, K_p , obtained for the peaks. This would better constrain this velocity and allow the reliability of the detections

obtained at extreme values of planetary orbital velocity to be investigated.

Further work could also be done to investigate the abundances of the chemical species detected and the temperature of these species. This information could then be used to compare with other bloated hot-Jupiters. This would help further our understanding of the properties of this class of exoplanet.

Another aspect that could be investigated is the change in blueshift of the signal throughout the transit of WASP-76b. Doing this would provide more detail on the nature of the winds in the atmosphere, and could help further the understanding of the climates on ultra hot gas giants. Comparing the results from this type of analysis with previous work such as that of Ehrenreich et al.(2020) [6], could also help investigate the presence of weather on ultra hot gas giants. Currently, we can only investigate climate in exoplanetary atmospheres. However, if we make multiple measurements of atmospheric properties, such as wind and chemical composition, we can begin to build a bigger picture and possibly gain insight into weather patterns in these types of atmospheres.

4 Conclusions

In this work, the transmission spectra obtained of WASP-76b using ESPRESSO at the VLT, were analysed using Doppler resolved transmission spectroscopy and cross correlation techniques. Using these methods, a number of atmospheric species were searched for in the atmosphere of WASP-76b. It was possible to detect the presence of FeI, NaI LiI, KI and MnI, which strengthens the previous detections of these species in other works [6][17][22]. It was possible to also detect features of FeII, TiI and CrI, which have not been reported in previous studies.

The transmission spectra were also analysed for the presence of MgI, NiI and CaII, however these searches were unsuccessful. This implies that these species are either not present in the atmosphere of WASP-76b, or their intensity is well below the minimum noise level of the observations.

It was found that the spectral features of these species were blueshifted with respect to the planetary rest frame. This is most likely due to strong planetary wind in the atmosphere, blowing from the hot day-side of the planet to the cooler night-side.

References

- [1] Ashok Ambardar. *Analog and digital signal processing*. 2nd. Pacific Grove ; London: Brooks/Coles, 1999. ISBN: 053495409x.
- [2] NASA Exoplanet Archive. *Retrieved 15 March 2021*. URL: exoplanetarchive.ipac.caltech.edu.
- [3] Isabelle Baraffe et al. “New evolutionary models for pre-main sequence and main sequence low-mass stars down to the hydrogen-burning limit”. In: *Astronomy & Astrophysics* 577, A42 (May 2015). DOI: 10.1051/0004-6361/201425481. arXiv: 1503.04107.
- [4] G. H. A. Cole and M. M. Woolfson. *Planetary science : the science of planets around stars*. Bristol: Institute of Physics Pub, 2002. ISBN: 075030815X.
- [5] Amanda P. Doyle et al. “Accurate spectroscopic parameters of WASP planet host stars”. In: *Monthly Notices of the Royal Astronomical Society* 428.4 (Feb. 2013), pp. 3164–3172. DOI: 10.1093/mnras/sts267. arXiv: 1210.5931.
- [6] D. Ehrenreich et al. “Nightside condensation of iron in an ultrahot giant exoplanet”. In: *Nature* 580.7805 (2020), p. 597. ISSN: 0028-0836. DOI: 10.1038/s41586-020-2107-1.
- [7] N. P. Gibson et al. “Detection of Fe I in the atmosphere of the ultra-hot Jupiter WASP-121b, and a new likelihood-based approach for Doppler-resolved spectroscopy”. In: *Monthly Notices of the Royal Astronomical Society* 493.2 (2020), pp. 2215–2228. ISSN: 0035-8711. DOI: 10.1093/mnras/staa228.
- [8] Carole Haswell. *Transiting exoplanets*. Cambridge: Cambridge University Press, 2010.
- [9] K. Heng and D. Kitzmann. “The theory of transmission spectra revisited: a semi-analytical method for interpreting WFC3 data and an unresolved challenge”. In: *Monthly Notices of the Royal Astronomical Society* 470.3 (2017), pp. 2972–2981. ISSN: 0035-8711. DOI: 10.1093/mnras/stx1453.
- [10] Laura Kreidberg. “Exoplanet Atmosphere Measurements from Transmission Spectroscopy and other Planet-Star Combined Light Observations”. In: *arXiv preprint arXiv:1709.05941* (2017).
- [11] Jack Jonathan Lissauer and Imke De Pater. *Fundamental planetary sciences : physics, chemistry and habitability*. Updated edition. Cambridge: Cambridge University Press, 2019. ISBN: 9781108411981.
- [12] Nikku Madhusudhan. “Exoplanetary Atmospheres: Key Insights, Challenges, and Prospects”. In: *Annual Review of Astronomy and Astrophysics* 57 (Aug. 2019), pp. 617–663. DOI: 10.1146/annurev-astro-081817-051846. arXiv: 1904.03190.
- [13] Michel Mayor and Didier Queloz. “A Jupiter-mass companion to a solar-type star”. In: *Nature* 378.6555 (Nov. 1995), pp. 355–359. DOI: 10.1038/378355a0.
- [14] M. A. C. Perryman. *The exoplanet handbook*. Second edition. Cambridge University Press, 2018. ISBN: 9781108419772.
- [15] F. Pont et al. “Detection of atmospheric haze on an extrasolar planet: the 0.55-1.05 μm transmission spectrum of HD 189733b with the HubbleSpaceTelescope”. In: *Monthly Notices of the Royal Astronomical Society* 385.1 (Mar. 2008), pp. 109–118. DOI: 10.1111/j.1365-2966.2008.12852.x. arXiv: 0712.1374.

- [16] David K Sing et al. “A continuum from clear to cloudy hot-Jupiter exoplanets without primordial water depletion”. In: *Nature* 529.7584 (2016), pp. 59–62.
- [17] H. M. Tabernero et al. “ESPRESSO high resolution transmission spectroscopy of WASP-76b”. In: *arXiv e-prints* (Nov. 2020), arXiv:2011.12197.
- [18] O. Tamuz, T. Mazeh, and S. Zucker. “Correcting systematic effects in a large set of photometric light curves”. In: *Monthly Notices of the Royal Astronomical Society* 356.4 (Feb. 2005), pp. 1466–1470. DOI: 10.1111/j.1365-2966.2004.08585.x. arXiv: astro-ph/0502056.
- [19] RG West et al. “Three irradiated and bloated hot Jupiters:-WASP-76b, WASP-82b, and WASP-90b”. In: *Astronomy & Astrophysics* 585 (2016), A126.
- [20] A. Wolszczan and D. A. Frail. “A planetary system around the millisecond pulsar PSR1257 + 12”. In: *Nature* 355.6356 (Jan. 1992), pp. 145–147. DOI: 10.1038/355145a0.
- [21] Hugh D. Young et al. *Sears and Zemansky’s University physics with modern physics*. Fourteenth edition, Global edition. Harlow, England: Pearson Education Limited, 2016. ISBN: 9781292100319.
- [22] Jiri Zak et al. “High-resolution transmission spectroscopy of four hot inflated gas giant exoplanets”. In: *The Astronomical Journal* 158.3 (2019), p. 120.

Appendices

A Peaks from Planetary Orbital vs Systemic Velocity Maps

A.1 FeI

Cloud Pressure (bar)	K_p (km/s)	v_{sys} (km/s)	σ
2000K			
1×10^{-1}	170	-8	8.0
1×10^{-2}	173	-8	7.3
1×10^{-3}	174	-8	5.8
1×10^{-4}	59	38	4.9
1×10^{-5}	59	-61	4.3
1×10^{-6}	234	-41	4.5
3000K			
1×10^{-1}	170	-8	8.0
1×10^{-2}	173	-8	7.3
1×10^{-3}	174	-8	5.8
1×10^{-4}	59	38	4.9
1×10^{-5}	59	-61	4.3
1×10^{-6}	234	-41	4.8
3500K			
1×10^{-1}	170	-8	8.0
1×10^{-2}	173	-8	7.3
1×10^{-3}	174	-8	5.8
1×10^{-4}	59	38	4.9
1×10^{-5}	59	-61	4.3
1×10^{-6}	222	-72	5.4
4000K			
1×10^{-1}	170	-8	8.0
1×10^{-2}	173	-8	7.3
1×10^{-3}	174	-8	5.8
1×10^{-4}	59	38	4.9
1×10^{-5}	59	-61	4.3
1×10^{-6}	223	-72	5.1

A.2 NaI

Cloud Pressure (bar)	K_p (km/s)	v_{sys} (km/s)	σ
2000K			
1×10^{-1}	191	-6	6.7
1×10^{-2}	194	-4	7.6
1×10^{-3}	194	-4	7.6
1×10^{-4}	189	-5	7.2
1×10^{-5}	189	-4	6.2
1×10^{-6}	195	-5	5.8
3000K			
1×10^{-1}	-224	72	5.5
1×10^{-2}	182	-8	6.2
1×10^{-3}	192	-6	6.8
1×10^{-4}	192	-4	7.2
1×10^{-5}	190	-5	6.4
1×10^{-6}	190	-5	5.9
3500K			
1×10^{-1}	-223	72	5.2
1×10^{-2}	191	-7	5.9
1×10^{-3}	182	-8	6.6
1×10^{-4}	191	-5	6.9
1×10^{-5}	191	-4	6.4
1×10^{-6}	190	-5	6.0
4000K			
1×10^{-1}	-222	72	4.9
1×10^{-2}	191	-8	5.5
1×10^{-3}	182	-8	6.4
1×10^{-4}	191	-6	6.7
1×10^{-5}	192	-4	6.4
1×10^{-6}	190	-5	6.1

A.3 LiI

Cloud Pressure (bar)	K_p (km/s)	v_{sys} (km/s)	σ
2000K			
1×10^{-1}	-266	95	6.0
1×10^{-2}	-286	103	5.5
1×10^{-3}	-225	81	5.8
1×10^{-4}	115	-5	5.6
1×10^{-5}	118	-6	5.6
1×10^{-6}	123	-6	5.8
3000K			
1×10^{-1}	-268	96	5.4
1×10^{-2}	-247	96	5.2
1×10^{-3}	-227	88	5.9
1×10^{-4}	84	8	5.3
1×10^{-5}	113	-4	5.5
1×10^{-6}	116	-5	5.5
3500K			
1×10^{-1}	-269	96	5.0
1×10^{-2}	263	-14	5.2
1×10^{-3}	-226	88	5.8
1×10^{-4}	-230	87	5.3
1×10^{-5}	113	-4	5.2
1×10^{-6}	114	-5	5.4
4000K			
1×10^{-1}	257	-12	4.7
1×10^{-2}	260	-13	5.1
1×10^{-3}	262	-15	5.8
1×10^{-4}	-226	88	5.4
1×10^{-5}	-201	74	5.2
1×10^{-6}	113	-4	5.4

A.4 KI

Cloud Pressure (bar)	K_p (km/s)	v_{sys} (km/s)	σ
2000K			
1×10^{-1}	-135	113	4.8
1×10^{-2}	214	-12	4.6
1×10^{-3}	212	-12	5.2
1×10^{-4}	212	-12	6.0
1×10^{-5}	177	-10	5.8
1×10^{-6}	177	-9	5.7
3000K			
1×10^{-1}	-138	114	4.1
1×10^{-2}	221	-11	3.6
1×10^{-3}	214	-12	4.0
1×10^{-4}	212	-12	4.9
1×10^{-5}	179	-10	5.5
1×10^{-6}	178	-10	5.8
3500K			
1×10^{-1}	-139	114	3.9
1×10^{-2}	-138	113	3.3
1×10^{-3}	221	-11	3.6
1×10^{-4}	211	-12	4.5
1×10^{-5}	179	-10	4.9
1×10^{-6}	179	-10	5.8
4000K			
1×10^{-1}	-140	114	3.8
1×10^{-2}	-139	114	3.3
1×10^{-3}	-138	113	3.3
1×10^{-4}	211	-12	4.2
1×10^{-5}	211	-12	4.4
1×10^{-6}	179	-10	5.8

A.5 TiI

Cloud Pressure (bar)	K_p (km/s)	v_{sys} (km/s)	σ
2000K			
1×10^{-1}	219	-37	4.4
1×10^{-2}	220	-37	4.5
1×10^{-3}	-165	25	4.3
1×10^{-4}	-271	54	4.5
1×10^{-5}	-300	42	4.3
1×10^{-6}	-298	43	4.4
3000K			
1×10^{-1}	200	-6	4.2
1×10^{-2}	120	2	4.3
1×10^{-3}	122	1	4.3
1×10^{-4}	-115	104	4.6
1×10^{-5}	-116	104	4.6
1×10^{-6}	-300	42	4.7
3500K			
1×10^{-1}	199	-7	4.3
1×10^{-2}	119	2	4.2
1×10^{-3}	122	1	4.5
1×10^{-4}	153	-76	4.8
1×10^{-5}	-115	104	4.8
1×10^{-6}	-300	42	4.8
4000K			
1×10^{-1}	212	-8	4.6
1×10^{-2}	142	-8	4.4
1×10^{-3}	122	1	4.5
1×10^{-4}	153	-76	4.6
1×10^{-5}	-114	104	5.0
1×10^{-6}	-116	104	5.0

A.6 MnI

Cloud Pressure (bar)	K_p (km/s)	v_{sys} (km/s)	σ
2000K			
1×10^{-1}	207	-9	5.6
1×10^{-2}	155	-11	5.1
1×10^{-3}	158	-12	5.0
1×10^{-4}	96	-63	5.3
1×10^{-5}	98	-63	4.9
1×10^{-6}	-227	59	5.1
3000K			
1×10^{-1}	224	-16	6.4
1×10^{-2}	220	-16	6.2
1×10^{-3}	208	-9	5.5
1×10^{-4}	209	-9	5.0
1×10^{-5}	97	-63	5.0
1×10^{-6}	-226	59	5.0
3500K			
1×10^{-1}	225	-16	5.9
1×10^{-2}	223	-16	6.4
1×10^{-3}	221	-16	5.9
1×10^{-4}	207	-9	5.2
1×10^{-5}	96	-63	5.2
1×10^{-6}	-226	59	4.9
4000K			
1×10^{-1}	212	-11	5.6
1×10^{-2}	224	-16	6.0
1×10^{-3}	222	-16	6.1
1×10^{-4}	208	-9	5.3
1×10^{-5}	-262	77	4.8
1×10^{-6}	-226	59	4.9

A.7 CrI

Cloud Pressure (bar)	K_p (km/s)	v_{sys} (km/s)	σ
2000K			
1×10^{-1}	188	-7	4.4
1×10^{-2}	221	-4	4.7
1×10^{-3}	257	-2	4.5
1×10^{-4}	256	-3	4.7
1×10^{-5}	-111	70	4.5
1×10^{-6}	-111	70	4.3
3000K			
1×10^{-1}	194	-13	6.0
1×10^{-2}	194	-13	5.1
1×10^{-3}	236	7	4.4
1×10^{-4}	221	-4	4.7
1×10^{-5}	256	-3	4.6
1×10^{-6}	-111	70	4.5
3500K			
1×10^{-1}	196	-14	5.8
1×10^{-2}	195	-13	5.8
1×10^{-3}	236	7	5.1
1×10^{-4}	221	-4	4.5
1×10^{-5}	256	-3	4.6
1×10^{-6}	-111	70	4.4
4000K			
1×10^{-1}	176	-7	5.3
1×10^{-2}	195	-13	5.8
1×10^{-3}	236	7	5.5
1×10^{-4}	236	7	4.8
1×10^{-5}	258	-2	4.4
1×10^{-6}	-111	70	4.4

A.8 MgI

Cloud Pressure (bar)	K_p (km/s)	v_{sys} (km/s)	σ
2000K			
1×10^{-1}	-168	-58	5.2
1×10^{-2}	-168	-57	6.2
1×10^{-3}	-167	-57	6.7
1×10^{-4}	-131	-58	6.2
1×10^{-5}	-	-	-
1×10^{-6}	-	-	-
3000K			
1×10^{-1}	-126	-77	4.4
1×10^{-2}	-140	-78	5.0
1×10^{-3}	-141	-78	5.6
1×10^{-4}	-143	-79	5.6
1×10^{-5}	-42	-71	5.7
1×10^{-6}	-	-	-
3500K			
1×10^{-1}	206	-114	4.4
1×10^{-2}	-135	-78	4.6
1×10^{-3}	-140	-78	5.4
1×10^{-4}	-129	-81	5.6
1×10^{-5}	-129	-80	5.7
1×10^{-6}	80	-81	5.9
4000K			
1×10^{-1}	208	-115	4.4
1×10^{-2}	-134	-78	4.6
1×10^{-3}	-138	-78	5.4
1×10^{-4}	-130	-80	5.6
1×10^{-5}	-129	-80	5.7
1×10^{-6}	-42	-72	5.9

A.9 CaII

Cloud Pressure (bar)	K_p (km/s)	v_{sys} (km/s)	σ
2000K			
1×10^{-1}	259	-35	5.1
1×10^{-2}	278	74	3.6
1×10^{-3}	183	89	3.2
1×10^{-4}	-62	120	4.6
1×10^{-5}	-33	117	5.1
1×10^{-6}	-32	117	4.9
3000K			
1×10^{-1}	92	83	5.0
1×10^{-2}	188	89	3.4
1×10^{-3}	-62	120	3.3
1×10^{-4}	-62	120	4.7
1×10^{-5}	-35	117	5.1
1×10^{-6}	-32	117	4.9
3500K			
1×10^{-1}	92	83	4.9
1×10^{-2}	188	89	3.6
1×10^{-3}	-62	120	3.4
1×10^{-4}	-62	120	4.7
1×10^{-5}	-62	120	5.2
1×10^{-6}	-35	117	4.9
4000K			
1×10^{-1}	93	83	4.9
1×10^{-2}	188	89	3.3
1×10^{-3}	-62	120	3.4
1×10^{-4}	-62	120	4.8
1×10^{-5}	-62	120	5.2
1×10^{-6}	-36	117	5.0

A.10 NiI

Cloud Pressure (bar)	K_p (km/s)	v_{sys} (km/s)	σ
2000K			
1×10^{-1}	259	-61	4.8
1×10^{-2}	-92	78	5.0
1×10^{-3}	92	50	4.7
1×10^{-4}	182	-33	4.9
1×10^{-5}	110	-36	5.6
1×10^{-6}	110	-36	5.4
3000K			
1×10^{-1}	-69	93	4.6
1×10^{-2}	-171	99	4.3
1×10^{-3}	246	-62	4.6
1×10^{-4}	177	-51	4.9
1×10^{-5}	189	-31	5.6
1×10^{-6}	110	-36	5.6
3500K			
1×10^{-1}	-155	51	4.5
1×10^{-2}	-204	84	4.4
1×10^{-3}	161	-43	4.4
1×10^{-4}	267	-90	4.5
1×10^{-5}	112	-36	5.0
1×10^{-6}	110	-36	5.6
4000K			
1×10^{-1}	-155	50	4.4
1×10^{-2}	-155	51	4.5
1×10^{-3}	-72	-51	4.4
1×10^{-4}	266	-90	4.8
1×10^{-5}	247	-62	4.6
1×10^{-6}	110	-36	5.6

A.11 FeII

Cloud Pressure (bar)	K_p (km/s)	v_{sys} (km/s)	σ
2000K			
1000×10^{-1}	-219	46	5.4
1000×10^{-2}	-271	-8	5.5
1000×10^{-3}	-177	-34	5.9
1000×10^{-4}	-	-	-
1000×10^{-5}	-	-	-
1000×10^{-6}	-	-	-
3000K			
1000×10^{-1}	241	6	4.4
1000×10^{-2}	194	-75	4.2
1000×10^{-3}	265	37	4.8
1000×10^{-4}	245	-34	4.3
1000×10^{-5}	228	-2	5.7
1000×10^{-6}	-	-	-
3500K			
1000×10^{-1}	63	-13	4.4
1000×10^{-2}	-219	7	4.1
1000×10^{-3}	265	-37	4.4
1000×10^{-4}	265	-37	4.6
1000×10^{-5}	-63	71	4.6
1000×10^{-6}	-	-	-
4000K			
1000×10^{-1}	63	-14	4.5
1000×10^{-2}	63	-14	4.0
1000×10^{-3}	195	-75	4.6
1000×10^{-4}	265	-37	4.8
1000×10^{-5}	245	-34	4.2
1000×10^{-6}	227	-2	6.0

B Astronomical Constants

Table 2: Astronomical constants used throughout this project in SI units.[4]

Solar Radius	R_{\odot}	$6.96 \times 10^8 \text{m}$
Solar Mass	M_{\odot}	$1.99 \times 10^{30} \text{kg}$
Earth Radius	R_{\oplus}	$6.38 \times 10^6 \text{m}$
Earth Mass	M_{\oplus}	$5.97 \times 10^{24} \text{kg}$
Jupiter Radius	R_{Jup}	$7.14 \times 10^7 \text{m}$
Jupiter Mass	M_{Jup}	$1.899 \times 10^{27} \text{kg}$
Astronomical unit	AU	$1.496 \times 10^{11} \text{m}$
Parsec	pc	$3.09 \times 10^{16} \text{m}$

C Sample Model Transmission Spectra

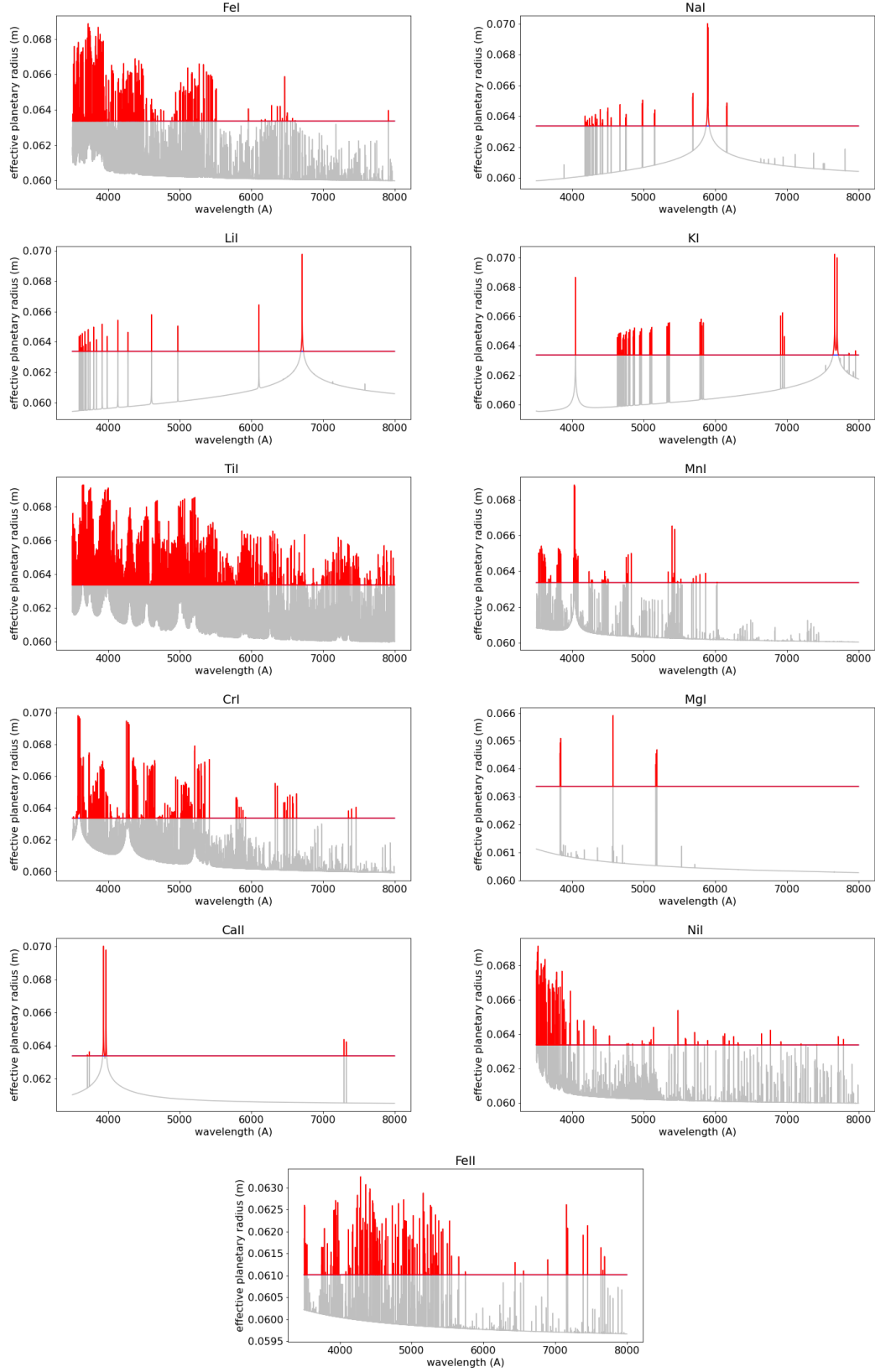


Figure 9: Model transmission spectra for each species. All with a temperature of 2000K and cloud deck at a pressure of 1×10^{-1} bar, apart from FeII, which has a cloud deck at a pressure of 1000×10^{-1} bar.